CrossMark

RESEARCH PAPER

A mathematical model for nanoparticle melting with size-dependent latent heat and melt temperature

H. Ribera[1,2] · T. G. Myers[1,2]

Abstract In this paper, we study the melting of a spherical nanoparticle. The model differs from previous ones in that a number of features have been incorporated to match experimental observations. These include the size dependence of the latent heat and a cooling condition at the boundary (as opposed to the fixed temperature condition used in previous studies). Melt temperature variation and density change are also included. The density variation drives the flow of the outer fluid layer. The latent heat variation is modelled by a new relation, which matches experimental data better than previous models. A novel form of Stefan condition is used to determine the position of the melt front. This condition takes into account the latent heat variation, the energy required to create new surface and the kinetic energy of the displaced fluid layer. Results show that melting times can be significantly faster than predicted by previous theoretical models; for smaller particles, this can be around a factor 3. This is primarily due to the latent heat variation. The previously used fixed temperature boundary condition had two opposing effects on melt times: the implied infinite heat transfer led to faster melting but also artificially magnified the effect of kinetic energy, which slowed down the process. We conclude that any future models of nanoparticle melting must be based on the new Stefan condition and account for latent heat variation.

1 Introduction

Nanoparticles are currently the focus of extensive research due to their unique properties and their applications in many fields. They are used in medicine, for both diagnosis and drug delivery (Mornet et al. 2004; Yih and Al-Fandi 2006), in biology (Salata 2004) and in optics (Ahmad et al. 2012). They are also used to increase efficiency in energy production, in the creation of new optoelectronic devices (Tanabe 2007) and in materials with modified properties (Dieringer et al. 2006; Gröhn et al. 2001). In many of these applications, high temperatures are involved, so it is important to understand how nanoparticles respond to heat and how they behave if a phase change occurs.

Nanoparticles have a high ratio of surface to volume atoms, which makes them behave differently to their bulk counterparts: examples include enhanced mechanical strength; enhanced solar radiation absorption and superparamagnetism. A well-known nanoscale property is the decrease in the phase change temperature with particle size. Buffat and Borel (1976) reported a decrease of approximately 500 K below the bulk melt temperature (approximately 60 %) for gold nanoparticles with radii a little above 1 nm. Decreases of 70 and 200 K have been reported for tin and lead nanoparticles (David et al. 1995). The variation in surface tension with radius has been approximated by the relation $\sigma_{sl} = \sigma_{sl}^*(1 - 2\delta/R)$ (Tolman 1949), where σ_{sl} is the surface tension, the star denotes the bulk value, δ is termed the Tolman length and R is the particle radius. The Tolman length is typically very small: in this paper we will use data for tin with $\delta = 0.373$ nm. This value leads to

✉ T. G. Myers
tmyers@crm.cat

1 Centre de Recerca Matemàtica, Campus de Bellaterra, Edifici C, Bellaterra, 08193 Barcelona, Spain

2 Department de Matemàtica Aplicada, Universitat Politècnica de Catalunya, Barcelona, Spain

a decrease in surface tension of approximately 15 % from the bulk value for a particle of radius 5 nm and 1 % for a particle of radius 100 nm.

Molecular dynamics (MD) simulations and experiments have also demonstrated a decrease in latent heat with a decrease in radius. Lai et al. (1996) presented the first calorimetry measurements of the melting process of nanometre-sized tin particles, ranging from $5 - 50$ nm in diameter. They found a reduction of up to 70 % from the bulk latent heat for the smaller-sized particles. Jiang et al. (2006) improved the measurement technique to find even greater reductions. Using a thin-film scanning calorimetry technique, similar behaviour was observed by Zhang et al. (2000) in a study of the melting behaviour of $0.1 - 10$ nm-thick discontinuous indium films made from ensembles of nanostructures. In the MD studies of Bachels et al. (2000), the melt temperature of 1.4-nm-radius tin particles is 25 % lower than the bulk value whilst the latent heat is 45 % lower. Ercolessi et al. (1991), Lim et al. (1993) and Delogu (2005) have carried out MD studies on gold, lead and copper clusters, all showing the same qualitative behaviour.

The mathematical modelling of phase change is termed the Stefan problem. Theoretical studies of Stefan problems involve a number of restrictive assumptions, made primarily for mathematical convenience, and so they really only apply to idealised situations. Standard assumptions include constant thermophysical properties in each phase and the same density in both phases, constant phase change temperature, latent heat and surface tension and also a fixed temperature boundary condition. A number of these assumptions are discussed in Alexiades and Solomon (1992, Table 1.1). Melting point depression (where the melt temperature decreases with particle size) was considered in the mathematical studies of Back et al. (2014a, b), Font and Myers (2013), Font et al. (2014), McCue et al. (2009), Wu et al. (2009a, b). McCue et al. (2009) propose this as the primary reason for the experimentally observed sudden disappearance of nanoparticles. In all of these studies, the outer boundary temperature was taken to be a constant (greater than the melt temperature). Font et al. (2014) included density variation and melting point depression in their model. They demonstrated that melt times increased with density variation and explained this through the energy required to move the liquid. They also demonstrated that a large contribution to this extra energy term came at the beginning of the process, as a result of the unrealistic fixed temperature boundary condition. The effect was most noticeable for small particles, but even as the size was allowed to tend to infinity, there was still a 15 % discrepancy (for gold at least) from the constant density model results. The thesis of Back (2016, §7.1–7.4) confirms this large discrepancy. It also includes a section where the latent heat employed in the standard energy balance is replaced by a size-dependent function, using a formula taken from Lai et al. (1996). This leads to a decrease in melt times. A converse problem, growth of nanoparticles, is considered in Dragomirescu et al. (2016). They investigate an ice-water system and use the standard Gibbs-Thomson relation, a single value for density, a fixed temperature boundary condition and a Stefan condition taken from models of macroscale melting. Growth and melting of nanowires are considered in Florio and Myers (2016). They also employ the standard Gibbs–Thomson relation and a constant density, at the boundary they consider both fixed temperature and cooling conditions. Their Stefan condition accounts for the energy required to make new surface. A significant feature of this work is that it demonstrates that solidification from the outer boundary is a faster process than melting.

Experiments and MD simulations have made it clear that both melt temperature and latent heat vary significantly during melting, with latent heat often showing the greatest variation. The surface tension variation is less noticeable. In practice, the boundary temperature cannot be instantaneously raised to some constant value. Consequently, in this paper we will attempt to extend the previous works to produce a more realistic melting model. Specifically, we will incorporate the variation of latent heat, melt temperature and density and impose a physically realistic boundary condition. One final novelty in this work concerns the form of Stefan condition. Previous studies on nanoparticle melting and the solidification of supercooled melts (Myers et al. 2012) use an energy balance (the Stefan condition) at the interface between the two phases which is based on an implicit assumption that the latent heat is released at the bulk melt temperature. Obviously this is not correct. In Myers (2016), a new form of Stefan condition is derived which involves an '*effective latent heat*', which is the sum of the size-dependent latent heat (released at the appropriate melt temperature), the kinetic energy and the energy required to make new surface.

In the following section, we will discuss the latent heat and propose a model to describe the variation with particle size. This will then be used in the development of the mathematical model, in Sect. 3. In Sect. 4, we apply an approximate solution method and verify the accuracy by comparison with the full numerical solution. In the results section, we demonstrate the effect of the various new components of the model which, for small particles, can lead to a factor three change in the predicted melt times. All equations are based on the validity of the continuum assumption. This has been discussed in detail in Font and Myers (2013), Myers et al. (2014). For phase change, the limit of validity appears to be around 2–5 nm, depending on the material.

2 Latent heat variation

The size dependence of a number of physical properties has often been modelled by functions involving $1/R$. These include the surface tension, the Gibbs–Thomson relation for the melt temperature and the Ostwald–Freundlich equation for a particle's solubility (it is also quoted for surface tension). Consequently, when investigating size-dependent properties at the nanoscale, it is standard to start with functions involving $1/R$. Recent investigations into the latent heat variation have led to the following relations.

Lai et al. (1996) suggest

$$L_m = L_m^* \left(1 - \frac{\delta_t}{R} \right)^3, \tag{1}$$

where L_m^* is the bulk latent heat. The constant δ_t was chosen to provide the best fit to their experimental data for melt temperature; for tin, they found $\delta_t = 16$ Å. Xiong et al. (2011) propose

$$L_m = L_m^* \left[1 + \left(1 + \frac{3R_G T_m^*}{2L_m^*} \right) \left(\frac{\pi N_A d^4 T_m^* b}{L_m^*} \right) \frac{1}{2R} \right], \tag{2}$$

where T_m^* is the bulk melt temperature, R_G is the gas constant, N_A Avogadro's number, d the atom diameter and b a negative constant that acts as a fitting parameter. Shin and Deinert (2014) model the latent heat by

$$L_m = L_m^* - \Delta h_s + \frac{2\sigma_{sl}}{\rho_s R} - \frac{2\sigma_{lv}(\rho_s - \rho_l)}{\rho_l \rho_s (R + \delta_t)}, \tag{3}$$

where Δh_s is the change in specific enthalpy, ρ_s, ρ_l are the density of the solid and liquid, σ_{lv} is the liquid–vapour surface tension. The change of the specific enthalpy of the solid is

$$\begin{aligned}
\Delta h_s = {} & \frac{1}{\rho_s} \left(\frac{2\sigma_{sl}}{R} + \frac{2\sigma_{lv}}{R + \delta_t} \right) + \frac{3\sigma_{sl}^*}{\rho_s R} - \frac{12\sigma_{sl}^* \delta}{\rho_s R^2} \\
& - T \left(\left(\frac{2\sigma_{sl}}{R} + \frac{2\sigma_{lv}}{R + \delta_t} \right) \frac{d(1/\rho_s)}{dT} \right. \\
& \left. + \frac{3}{\rho_s R} \frac{d\sigma_{sl}^*}{dT} - \frac{12\delta}{\rho_s R^2} \frac{d\sigma_{sl}^*}{dT} \right).
\end{aligned} \tag{4}$$

For tin nanoparticles, they define $\sigma_{sl} = 0.11\sigma_{lv}$ where σ_{sl} is defined by the Tolman relation with $\delta = 3.73 \times 10^{-10}$m and they take δ_t from Lai et al. (1996).

In Fig. 1, we compare the predictions of these relations with experimental data for the latent heat of tin, taken from Lai et al. (1996). The necessary parameter values are provided in Table 1. In Xiong et al. (2011), the fitting parameter b is calculated to provide a best fit with melt temperature data for different metals. They do not give a value for tin, so we performed a least-squares fit to the latent heat
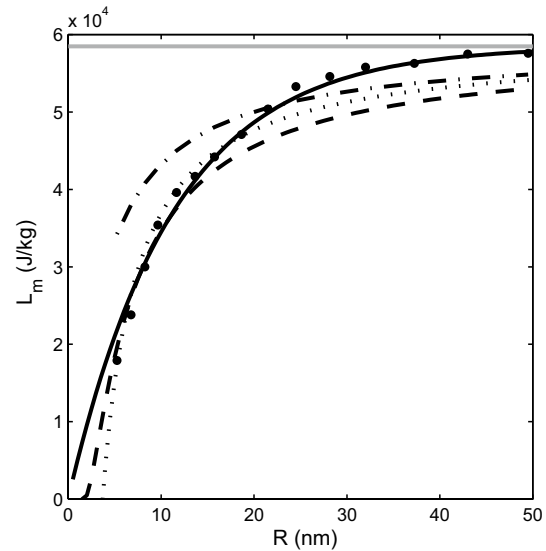

Fig. 1 Latent heat for a tin nanoparticle as a function of the radius. Lai et al. model [Eq. (1)], *dashed line*. Model proposed by Xiong et al. (2011) [Eq. (2)], *dotted line*. Shin and Deinert (2014) [Eq. (3)], *dash–dotted line*. Exponential fit proposed in this paper [Eq. (6)], *solid line*. Dots are experimental data of Lai et al. (1996). *Grey horizontal line* indicates bulk value

data; hence, our curve for latent heat variation using their formula is closer to the experimental data than theirs. We determined a value $b = -6.65 \times 10^{30}$(m K s^2)$^{-1}$; this is of the order of their quoted values for five other metals. The circles in the figure represent the experimental data, the dashed line that of Eq. (1), the dotted line that of Eq. (2) and the dash–dot line that of Eq. (3). The comparisons for melt temperature variation shown in the graphs of Lai et al. (1996), Xiong et al. (2011) demonstrate excellent agreement with the data, whilst the latent heat representation is poor, only matching the data points for the three smallest particles. In Fig. 1, this poor agreement may also be seen. In Shin and Deinert (2014), the results presented for latent heat show good agreement with data; unfortunately, we have been unable to reproduce this agreement.

The three previous theoretical models involve a single fitting parameter and so should exhibit some agreement with the data. However, a single fitting parameter restricts the ability of the model to accurately approximate data over a large range. The form of the models also ensures $L_m \to L_m^*$ as $R \to \infty$. A problem common to them all is the speed of decay to the bulk value. For sufficiently large R, they may all be expressed in the form

$$L_m(R) = L_m^* \left(1 - \frac{A_1}{R} + \frac{A_2}{R^2} + \cdots \right) \tag{5}$$

for various values of A_i. It would appear that this form of polynomial in $1/R$ does not exhibit the correct limiting behaviour. A particularly worrying feature of this

Table 1 Thermodynamical parameter values for tin, data taken from Bachels et al. (2000), Garg et al. (1993), (http://www.engineeringtool-box.com/latent-heat-melting-solids-d_96.html.), (http://www.engineer-ingtoolbox.com/thermal-conductivity-d_429.html.), Lai et al. (1996), Sharafat and Ghoniem (2000), Shin and Deinert (2014)

Material	T_m^* (K)	L_m^* (J/kg)	c_s/c_l (J/kg·K)	k_s/k_l (W/m·K)	ρ_s/ρ_l (kg/m³)	σ_{sl}^* (N/m)
Tin	505	58,500	230/268	67/30	7180/6980	0.064

observation is that the bulk value is the most reliable one, and the models clearly do not approach the only truly reliable data point correctly. Motivated by the inaccuracy of these models we propose a form that permits more rapid decay for large R,

$$L_m = L_m^* \left(1 - e^{-C\frac{R}{R_c}} \right), \tag{6}$$

where the constant C is our fitting parameter. To ensure C takes reasonable values we also introduce the capillary length $R_c = \sigma_{sl}^*/(\rho_s L_m^*)$. The solid curve shown in Fig. 1 represents our exponential relation, where the value $C = 0.0133$ has been used. This was obtained via a least-squares fit to the data. It is quite clear that the exponential relation is a significant improvement on the other models. For large radii, it is the only result that comes close to the experimental data. Below 15 nm three models, the current exponential, Lai's and Xiong's all provide a reasonable fit. Only below around 8 nm does our model show a noticeable deviation from the data. In the following sections, we will model nanoparticle melting with sizes varying between 2–100 nm. Consequently we will employ our exponential relation to describe latent heat variation, since this appears to be the only accurate relation for this range of particle radii.

3 Mathematical model

The physical situation considered in this section follows the standard form described in previous papers Font and Myers (2013), Font et al. (2014), McCue et al. (2009), (Wu et al. 2009a, b). A nanoparticle with initial radius R_0 is subjected to an external heat source which results in melting. The melting begins at the outer boundary and progresses inwards until the whole particle has melted. The solid–liquid interface is denoted $R(t)$. Since the liquid and solid densities are different the outer boundary moves, this is denoted $R_b(t)$, where $R_b(0) = R_0$. A sketch of this situation is presented in Fig. 2. The temperature in each phase is described by the standard heat equations

$$\rho_l c_l \left(\frac{\partial T}{\partial t} + v \frac{\partial T}{\partial r} \right) = k_l \frac{1}{r^2} \frac{\partial}{\partial r} \left(r^2 \frac{\partial T}{\partial r} \right), \quad R(t) < r < R_b(t), \tag{7}$$
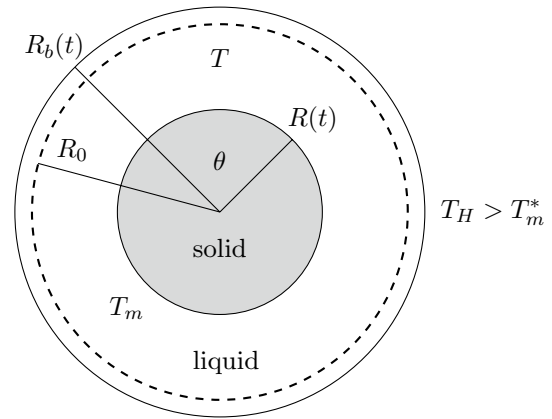

Fig. 2 Sketch of the problem

$$\rho_s c_s \frac{\partial \theta}{\partial t} = k_s \frac{1}{r^2} \frac{\partial}{\partial r} \left(r^2 \frac{\partial \theta}{\partial r} \right), \quad 0 < r < R(t), \tag{8}$$

where T and θ denote the temperature in the liquid and solid respectively, ρ_i, c_i and k_i are the densities, the specific heats and the conductivities respectively. The index notation $i = s$, l refers to the solid or liquid phases. The velocity v at which heat is advected in Eq. (7) is given by Font et al. (2014)

$$v = -\frac{R^2}{r^2} (\rho - 1) \frac{dR}{dt}, \tag{9}$$

where $\rho = \rho_s/\rho_l$.

The heat equation in the solid must be solved over the region $0 \leq r \leq R(t)$. The position of the melt front, $R(t)$, is determined by the energy balance

$$\left(\rho_s \left[L_m + \frac{v(R,t)^2}{2} \right] + \frac{2\sigma_{sl}^*}{R} \right) \frac{dR}{dt} = k_s \frac{\partial \theta}{\partial r} \bigg|_{r=R} - k_l \frac{\partial T}{\partial r} \bigg|_{r=R}. \tag{10}$$

This is the Stefan condition derived in Myers (2016). The terms in the brackets on the left-hand side represent the (time dependent) latent heat, the kinetic energy and the energy required to create new surface. The rate at which this energy is released, dR/dt, is balanced by the energy conducted through the solid and liquid. Note that the factor in brackets on the left-hand side differs significantly to

the one used in previous studies on nanoparticle melting, $\rho_s(L_m^* + (c_l - c_s)(T_m - T_m^*) + v^2/2)$. This latter version of the effective latent heat has been taken as standard when modelling nanoparticle melting and the solidification of supercooled materials (with the exception of Dragomirescu et al. (2016) who use $\rho_s L_m^*$). It is derived in Fedorov and Shulgin (2011), where they specify latent heat release at the bulk melt temperature T_m^*. Obviously latent heat is released at the appropriate size-dependent melt temperature. In Myers (2016), it is shown that the previous form of effective latent heat leads to errors (when compared to experimental data) up to a factor three for particles of the order 5 nm. Hence, in the following analysis we employ the relation (10).

The governing equations are subject to the boundary conditions

$$-k_l \frac{\partial T}{\partial r}\bigg|_{r=R_b} = h(T(R_b, t) - T_H), \quad T(R, t) = \theta(R, t)$$
$$= T_m(t), \quad \theta_r(0, t) = 0. \tag{11}$$

Note that at the outer boundary we specify a Newton cooling condition which states that the energy transferred to the particle is proportional to the temperature difference between the particle surface and the surrounding material. This is more physically realistic than the fixed temperature boundary condition, $T(R_b, t) = T_H$, which leads to an initial infinite boundary velocity. Following Font et al. (2014), we set the initial solid temperature to the melt temperature $\theta(r, 0) = T_m(0)$. This means that we avoid the issue of any initial heating up period, however, as we will see when the problem is non-dimensionalised heat flow is fast in comparison with the melting timescale so the imposition of any other temperature (below the melt temperature) would have little effect on the results.

The position of the outer boundary may be determined via the velocity relation. Setting $v(R_b) = dR_b/dt$ in Eq. (9) and integrating gives

$$R_b = \left(R_0^3 \rho - R^3(\rho - 1)\right)^{1/3}, \tag{12}$$

where $R(0) = R_b(0) = R_0$.

The fixed temperature boundary condition of previous studies is the limit of Eq. (11) as the heat transfer coefficient $h \to \infty$. Of course, this cannot be achieved physically and there exists a limit to the heat transfer beyond which the material would be vaporised. To permit comparison with previous models, we therefore choose the highest possible value for h which still permits thermodynamic stability. To do this, we set

$$h_{max} = \frac{q_{max}}{\Delta T}, \quad q_{max} = \rho_s u v_s, \tag{13}$$

where u is the internal energy and v_s is the speed of second sound in the material; see Florio and Myers (2016), Jou et al. (1996); ΔT is the temperature scale; here, we set $\Delta T = T_H - T_m^*$. A typical order of magnitude for h_{max} is found by first noting that the speed of second sound may be related to the phonon velocity $v_s = v_p/\sqrt{3}$. We follow Zhang et al. (2011) and take $v_p = \sqrt{B/\rho_s} \approx 2842$ m/s (B is the bulk modulus). The internal energy is given approximately by the enthalpy (this is valid under constant pressure, constant density and zero velocity), $u = c_s \Delta T$, consequently $h_{max} = \rho_s c_s v_s \approx 4.7 \times 10^9$ W/m^2 K. We will use this value in the following calculations since it will give the closest, physically achievable, comparison to previous fixed temperature results.

The melt temperature $T_m(t)$ may be approximated by the Gibbs–Thomson equation (Sun and Simon 2007),

$$T_m(t) = T_m^*\left(1 - \frac{2\sigma_{sl}^*}{\rho_s L_m^* R}\right). \tag{14}$$

Note that we use the bulk value σ_{sl}^* since the variation of surface tension is small (in comparison with the latent heat and melt temperature). This could be an obvious extension in subsequent work. Substituting the parameters from Table 1 into (14) we observe that $T_m(t)$ becomes negative for $R < 0.31$ nm. Taking into account that our model is valid for R where continuum theory holds, that is, $R > 2 - 5$ nm, the use of this version of the Gibbs–Thomson equation does not represent a problem.

We now scale the model using the dimensionless variables

$$\hat{T} = \frac{T - T_m^*}{\Delta T}, \quad \hat{\theta} = \frac{\theta - T_m^*}{\Delta T}, \quad \hat{T}_m = \frac{T_m - T_m^*}{\Delta T}, \quad \hat{L}_m = \frac{L_m}{L_m^*},$$
$$\hat{r} = \frac{r}{R_0}, \quad \hat{R} = \frac{R}{R_0}, \quad \hat{R}_b = \frac{R_b}{R_0}, \quad \hat{t} = \frac{k_l}{\rho_l c_l R_0^2}t. \tag{15}$$

This results in the following system (where we have immediately dropped the hat notation)

$$\frac{\partial T}{\partial t} - (\rho - 1)\frac{R^2}{r^2}\frac{dR}{dt}\frac{\partial T}{\partial r} = \frac{1}{r^2}\frac{\partial}{\partial r}\left(r^2\frac{\partial T}{\partial r}\right),$$
$$R(t) < r < R_b(t), \tag{16}$$

$$\frac{\partial \theta}{\partial t} = \frac{k}{\rho c}\frac{1}{r^2}\frac{\partial}{\partial r}\left(r^2\frac{\partial \theta}{\partial r}\right), \quad 0 < r < R(t), \tag{17}$$

where $k = k_s/k_l$, $c = c_s/c_l$ $R_b = \left(\rho - R^3(\rho - 1)\right)^{1/3}$ and $R_b(0) = R(0) = 1$. The boundary conditions are

$$\frac{\partial T}{\partial r}\bigg|_{r=R_b} = \Lambda(1 - T(R_b, t)), \quad T(R, t) = \theta(R, t) = T_m(t)$$
$$= -\frac{\Gamma}{R}, \quad \theta_r(0, t) = 0, \tag{18}$$

where $\Lambda = q_{max}R_0/(\Delta Tk_l), \Gamma = \alpha T_m^*/\Delta T$ and $\alpha = 2\sigma_{sl}^*/(\rho_s L_m^* R_0)$. The initial temperature becomes $\theta(r, 0) = -\Gamma$. The Stefan condition is

$$\rho\beta\left[L_m(t) + \frac{\alpha}{R}\right]\frac{dR}{dt} + \gamma\left(\frac{dR}{dt}\right)^3 = k\frac{\partial\theta}{\partial r}\bigg|_{r=R} - \frac{\partial T}{\partial r}\bigg|_{r=R},$$
(19)

where the Stefan number $\beta = L_m^*/(c_l\Delta T)$ and $\gamma = (1-\rho)^2 \rho_s\kappa_l^3/(2\Delta Tk_lR_0^2)$, where $\kappa_l = k_l/(\rho_lc_l)$ is the thermal diffusivity.

The Stefan number, β, depends on the temperature scale of the process: it is large for a small temperature variation and small for a large temperature variation. As we are working at the nanoscale, the Stefan number is typically large since, due to melting point depression, only a very small increase above the melt temperature is sufficient to induce complete particle melting. By the same argument, one may assume $\gamma \gg 1$; however, diffusion coefficients are typically small, for the present case $\kappa_l \approx 1.6 \times 10^{-5}$, so ensuring γ remains small. With $\Delta T = 10$K and $R_0 = 10$nm we obtain $\gamma \approx 0.4$. The value decreases for larger values of R_0 and ΔT.

4 Perturbation solution

The beauty of an analytical or approximate analytical solution is that it makes clear the factors driving a physical process in a manner that cannot be achieved by a numerical solution. Consequently we now follow previous researchers in using a perturbation method based on the large Stefan number.

If we consider Eq. (19) and divide through by β, then we find $dR/dt \approx 0$ (for sufficiently large β). Physically this tells us that the large Stefan number solution corresponds to slow melting (slow compared to the heat transfer in the material). Since we wish to focus on the melting, we therefore rescale time via $\tau = \epsilon t$ where $\epsilon = 1/\beta \ll 1$. The Stefan condition may now be written

$$\rho\left[L_m(t) + \frac{\alpha}{R}\right]\frac{dR}{d\tau} + \gamma\epsilon^3\left(\frac{dR}{d\tau}\right)^3 = k\frac{\partial\theta}{\partial r}\bigg|_{r=R} - \frac{\partial T}{\partial r}\bigg|_{r=R}.$$
(20)

With the new timescale, the time derivatives in the two heat equations, Eqs. (16, 17), are now multiplied by ϵ. So now, on the timescale of melting, the heat equations are close to a pseudo-steady state. It is not a true steady state since the boundary conditions still depend on time. Physically this means that as the melting proceeds, the temperature adjusts so rapidly that it appears to take the appropriate steady-state form. This is the justification for our earlier statement

that the initial solid temperature does not have a significant effect on the final results.

To solve the system, we can look for an expansion for the temperatures of the form $T = T_0 + \epsilon T_1 + \mathcal{O}(\epsilon^2)$. At order ϵ^0 we find the temperature in the liquid is described by

$$0 = \frac{1}{r^2}\frac{\partial}{\partial r}\left(r^2\frac{\partial T_0}{\partial r}\right), \quad \frac{\partial T_0}{\partial r}\bigg|_{r=R_b} = \Lambda(1 - T_0(R_b, \tau)),$$
$$T_0(R, \tau) = -\frac{\Gamma}{R},$$
(21)

At order ϵ^1 the temperature is described by

$$\frac{\partial T_0}{\partial\tau} - (\rho - 1)\frac{R^2}{r^2}\frac{dR}{d\tau}\frac{dT_0}{dr} = \frac{1}{r^2}\frac{\partial}{\partial r}\left(r^2\frac{\partial T_1}{\partial r}\right),$$
$$\frac{\partial T_1}{\partial r}\bigg|_{r=R_b} = -\Lambda T_1(R_b, \tau), \quad T_1(R, \tau) = 0.$$
(22)

The appropriate solution is

$$T_0(r, \tau) = F_1(\tau) + \frac{F_2(\tau)}{r},$$
(23)

$$T_1(r, \tau) = \frac{r^2}{6}\frac{dF_1}{d\tau} + \frac{r}{2}\frac{dF_2}{d\tau} - \frac{F_3(\tau)}{r}$$
$$+ \frac{R^2R_\tau F_2(\tau)(\rho - 1)}{2r^2} + F_4(\tau),$$
(24)

where

$$F_1(\tau) = \frac{\Gamma(\Lambda R_b - 1) + \Lambda R_b^2}{-R(\Lambda R_b - 1) + \Lambda R_b^2},$$
(25)

$$F_2(\tau) = -\Gamma - F_1(\tau)R,$$
(26)

$$F_3(\tau) = \frac{R_b^2 R}{R - \Lambda R_b R + \Lambda R_b^2}\left[\frac{1}{6}\frac{dF_1}{d\tau}(\Lambda R^2 - \Lambda R_b^2 - 2R_b)\right.$$
$$+ \frac{1}{2}\frac{dF_2}{d\tau}(\Lambda R - \Lambda R_b - 1)$$
$$\left. + \frac{R_\tau F_2(\tau)(\rho - 1)}{2}\left(1 - \frac{\Lambda R^2}{R_b^2} + \frac{2R^2}{R_b^3}\right)\right],$$
(27)

$$F_4(\tau) = -\frac{R^2}{6}\frac{dF_1}{d\tau} - \frac{R}{2}\frac{dF_2}{d\tau} + \frac{F_3(\tau)}{R} - \frac{R_\tau F_2(\tau)(\rho - 1)}{2}.$$
(28)

Note that T_1, F_3, F_4 involve time derivatives of F_1, F_2. Both derivatives may be written in a form $R_\tau\overline{F}_i$ for appropriate functions $\overline{F}_i$, and consequently, the same is true for F_3, F_4.

Similarly, for the solid temperature we obtain

$$0 = \frac{k}{\rho c}\frac{1}{r^2}\frac{\partial}{\partial r}\left(r^2\frac{\partial\theta_0}{\partial r}\right), \quad \frac{\partial\theta_0}{\partial r}\bigg|_{r=0} = 0, \quad \theta_0(R, \tau) = -\frac{\Gamma}{R},$$
(29)

$$\frac{\partial \theta_0}{\partial \tau} = \frac{k}{\rho c} \frac{1}{r^2} \frac{\partial}{\partial r} \left(r^2 \frac{\partial \theta_1}{\partial r} \right), \quad \left. \frac{\partial \theta_1}{\partial r} \right|_{r=0} = 0, \quad \theta_1(R, \tau) = 0.$$
(30)

This has solution

$$\theta_0(r, \tau) = -\frac{\Gamma}{R}, \quad \theta_1(r, \tau) = \frac{\Gamma}{6} \frac{\rho c}{k} \left(\frac{r^2 - R^2}{R^2} \right) R_\tau.$$
(31)

These expressions may be substituted into the Stefan condition (20). Using the relations $F_{i_\tau} = R_\tau \overline{F}_i$, and rearranging, we obtain a cubic equation for speed of the melt front, R_τ,

$$\epsilon^3 \gamma \left(\frac{dR}{d\tau} \right)^3 + \left(\rho \left[L_m(t) + \frac{\alpha}{R} \right] \right.$$
$$\left. + \epsilon \left[\frac{R\overline{F}_1}{3} + \frac{\overline{F}_2}{2} + \frac{\overline{F}_3}{R^2} - \frac{F_2(\rho - 1)}{R} - \frac{\Gamma \rho c}{3R} \right] \right) \frac{dR}{d\tau} - \frac{F_2}{R^2} = 0.$$
(32)

Whilst seemingly complex this formulation should be compared to the original problem, consisting of two partial differential equations for the temperature, coupled to varying melt temperature and latent heat equations all to be solved over two *a priori* unknown time-dependent domains.

Since $\epsilon \ll 1$, we can infer a lot about the melting behaviour from the dominant terms,

$$\frac{dR}{d\tau} = \frac{F_2}{\rho R^2} \left[L_m(t) + \frac{\alpha}{R} \right]^{-1} \approx \frac{F_2}{\rho L_m R^2}.$$
(33)

For most materials, the term in square brackets is dominated by $L_m(t)$ (at least for R larger than order 1 nm); hence, we have neglected the surface tension term in the approximation. In dimensional form, this leads to the initial melt rate

$$\frac{dR}{dt} \approx -\frac{q_m}{\rho_s L_m R_0^2}.$$
(34)

This equation is obtained by substituting for F_2, setting $R = R_b = 1$ and neglecting surface tension. It states that the initial melt rate is proportional to the heat flux and inversely proportional to the value of latent heat and square of the radius: smaller particles melt at a much faster rate than larger ones. If we had employed the fixed temperature boundary condition, there would be a factor $1/(R_0 - R)$ on the right-hand side. Since $R(0) = R_0$, this results in an infinite initial melt rate. This term is not present in Eq. (34) showing that the initial melt rate is in fact finite (as should be expected).

However, if we wish to follow the whole evolution process, then we must solve the cubic equation (particularly since we expect $dR/d\tau$ to become large near the end of the melting process). This is a simple matter, and we used MATLAB routines to solve the cubic and then integrate the resultant first-order differential equation for $R(\tau)$, subject

to the initial condition $R(0) = 1$. In the following section, we will describe the numerical solution method employed for the full problem and then compare with our results for solving the above cubic equation, leading to the conclusion that the cubic equation is sufficiently accurate.

5 Numerical solution

To verify the accuracy of the perturbation solution, we now describe a numerical scheme to solve the full problem with all terms retained. To do so, we follow the work in Font et al. (2014), so we define $u = rT$ and $v = r\theta$ and immobilise the boundaries on $r \in (R, R_b)$ via $\eta = (r - R)/(1 - R)$ and on $r \in (0, R)$ via $\zeta = r/R$. The problem (16)–(19) may now be written

$$\frac{\partial u}{\partial t} = -\eta_t \frac{\partial u}{\partial \eta} + \frac{1}{(R_b - R)^2} \frac{\partial^2 u}{\partial \eta^2}$$
$$- (1 - \rho) \frac{R^2}{(\eta(R_b - R) + R)^2}$$
$$\left(\frac{1}{R_b - R} \frac{\partial u}{\partial \eta} - \frac{u}{\eta(R_b - R) + R} \right) \frac{dR}{dt}, \quad 0 < \eta < 1,$$
(35)

$$\frac{\partial v}{\partial t} = -\zeta_t \frac{\partial v}{\partial \zeta} + \frac{1}{R^2} \frac{k}{\rho c} \frac{\partial^2 v}{\partial \zeta^2}, 0 < \zeta < 1.$$
(36)

The boundary conditions are

$$u(0, t) = -\Gamma,$$
$$\left. \frac{\partial u}{\partial \eta} \right|_{\eta=1} = u(1, t) \frac{(1 - \Lambda R_b)(R_b - R)}{R_b} \Lambda R_b(R_b - R),$$
$$v(0, t) = 0, \quad v(1, t) = -\Gamma.$$
(37)

The Stefan condition becomes

$$\rho \beta R[RL_m(t) + \alpha] \frac{dR}{dt} + \gamma R^2 \left(\frac{dR}{dt} \right)^3$$
$$= k \left. \frac{\partial v}{\partial \zeta} \right|_{\zeta=1} - \frac{R}{R_b - R} \left. \frac{\partial u}{\partial \eta} \right|_{\eta=0} + \Gamma(k - 1).$$
(38)

A semi-implicit finite difference method is used, whereby we solve implicitly for u and v and explicitly for R. The derivatives in (35)–(38) are approximated by

$$\frac{\partial u}{\partial t} = \frac{u_i^{n+1} - u_i^n}{\Delta t}, \quad \frac{\partial u}{\partial \eta} = \frac{u_{i+1}^{n+1} - u_{i-1}^{n+1}}{2\Delta \eta},$$
$$\frac{\partial^2 u}{\partial \eta^2} = \frac{u_{i+1}^{n+1} - 2u_i^{n+1} + u_{i-1}^{n+1}}{\Delta \eta^2},$$
(39)

where $i = 1, \ldots, J$ and $n = 1, \ldots, N$ and the derivatives for v are defined in the same manner. The position of the

melting front is obtained via the Stefan condition (38) using a three-point backward difference for the partial derivatives, and taking the time derivative to be

$$\frac{dR}{dt} = \frac{R^{n+1} - R^n}{\Delta t}. \qquad (40)$$

Finally, we obtain

$$a_i^n u_{i-1}^{n+1} + b_i^n u_i^{n+1} + c_i^n u_{i+1}^{n+1} = d^n u_i^n, \qquad (41)$$

$$e_i^n v_{i-1}^{n+1} + f^n v_i^{n+1} + g_i^n v_{i+1}^{n+1} = h^n v_i^n, \qquad (42)$$

for $i = 1, \ldots, J - 1$. For $i = J$,

$$\left(1 - \frac{(1 - \Lambda R_b^n)(R_b^n - R^n)\Delta x}{Rb}\right) u_i^{n+1} - u_{i-1}^{n+1} \\ = \Lambda R_b^n (R_b^n - R^n)\Delta x \quad \text{and} \quad v_i = 1. \qquad (43)$$

Equations (41) and (42) allow us to write down a matrix system which we solve at each time step n. For a more detailed description of the scheme, see Font et al. (2014).

5.1 Small time solution

A well-known difficulty encountered when solving Stefan problems numerically is that the liquid phase does not exist at $t = 0$ yet a numerical solution requires initial values. To overcome this in Font et al. (2014), a small time analysis is performed, which shows that as $t \to 0$, the radius takes the form $R \approx 1 - \lambda t^p$ where $p = 3/4$. This leads to an initial infinite velocity, $R_t \sim -t^{-1/4}$, which is a consequence of specifying a fixed temperature boundary condition. For the present problem, we use the same form, but leave p unknown. However, since we use a physically realistic boundary condition, we do not expect an infinite velocity, which then indicates $p \geq 1$. The imposed form for R leads to $R_b = 1 + (\rho - 1)\lambda t^p$, and so $R_b - R = \lambda \rho t^p$. Substituting these into Eq. (36), we obtain

$$(\lambda \rho t^p)^2 \frac{\partial u}{\partial t} = -(\lambda \rho t^p)^2 \eta_t \frac{\partial u}{\partial \eta} + \frac{\partial^2 u}{\partial \eta^2} \\ \qquad - (1 - \rho)\frac{(\lambda \rho t^p)(1 - \lambda t^p)^2}{(\lambda \rho t^p(\eta - 1) + 1)^2} \qquad (44) \\ \qquad \times \left(\frac{\partial u}{\partial \eta} - \frac{(\lambda \rho t^p) u}{\lambda \rho t^p(\eta - 1) + 1}\right)\frac{dR}{dt}, \quad 0 < \eta < 1.$$

Provided $p \geq 0$ all terms in the above expression tend to 0 as $t \to 0$ except for the second one on the right-hand side of the equation. This results in

$$\frac{\partial^2 u}{\partial \eta^2} \approx 0. \qquad (45)$$

Together with the boundary conditions for u given in (37), this leads to

$$u(\eta, t) \approx -\Gamma + \frac{(R_b - R)(\Lambda R_b^2 + \Lambda \Gamma R_b - \Gamma)}{\Lambda R_b^2 + R - \Lambda R_b R}\eta, \qquad (46)$$

which is the temperature in the liquid at small times.

The melting is driven by the heat flowing through the liquid; consequently, we may balance the left-hand side of the Stefan condition (38) with the temperature gradient in the liquid [which may be calculated using (46)]. Substituting for R, R_b and taking the Taylor series for $L_m(t) = L_m(0) + tL_m'(0) + \cdots$ and neglecting the terms involving t (since they tend to zero) we obtain

$$-\rho\beta[L_m(0) + \alpha]\lambda p t^{p-1} - \gamma \lambda^3 p^3 t^{3p-3} = -(\Lambda + \Lambda\Gamma - \Gamma). \qquad (47)$$

To balance with the right-hand side, which is independent of t, requires $p = 1$. This confirms that the initial velocity $R_t \approx -\lambda$ is finite. We have already shown that the kinetic energy term is small, it was retained in Font et al. (2014) because of the initial infinite velocity, in our finite velocity case we may neglect kinetic energy and so determine

$$\lambda = \frac{(\Lambda + \Lambda\Gamma - \Gamma)}{\rho\beta[L_m(0) + \alpha]}. \qquad (48)$$

Of course we could retain kinetic energy and then solve a cubic for λ, but this makes very little difference to the results.

6 Results

In this section, we present the results of the model. In all cases, we use data for tin, provided in Table 1, since we have already calculated an approximate exponential form for the latent heat variation in Sect. 2. Thermophysical data for gold nanoparticles may be found in the papers Font and Myers (2013), Font et al. (2014) (but without details of the latent heat variation). To permit comparison with a fixed boundary temperature model, we also impose the maximum heat flux discussed earlier.

To verify the analytical solution, we first compare it with predictions of the melt front position calculated using the numerical model. In Fig. 3, we plot the variation of the radius $R(t)$ for Stefan numbers $\beta = 10, 100$ (corresponding to $\Delta T = 22, 2.2$ K), initial radius $R_0 = 10, 100$ nm and a cooling condition with $h = h_{max} = 4.7 \times 10^9$ W/(m²K). The dashed lines represent the numerical solution described in Sect. 5. The solid lines come from the perturbation solution; calculated by solving the cubic Eq. (32) for R_τ and then integrating.

Note that we have plotted R down to the non-dimensional equivalent of 2 nm (i.e. when $R_0 = 10$ nm the
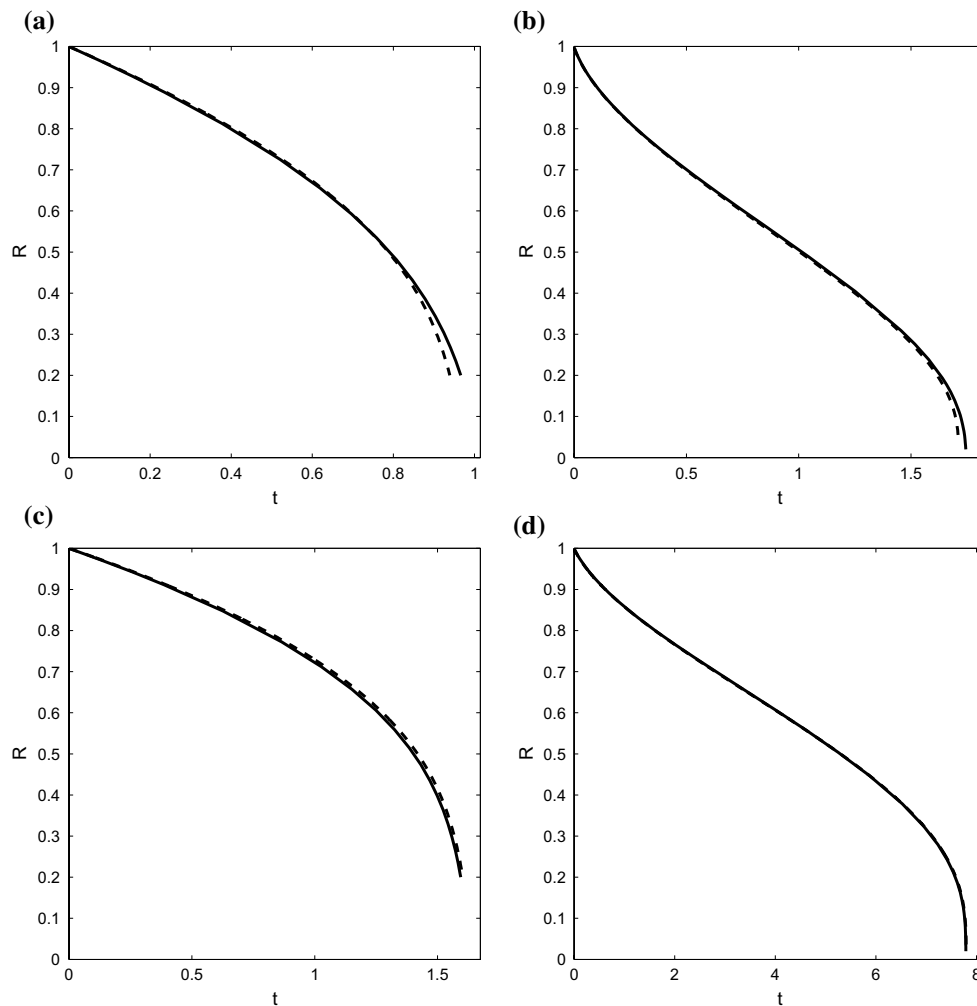
Fig. 3 Melting front evolution of a tin nanoparticle for perturbation (*solid line*) and numerical (*dashed line*) solutions for various β and R_0. The timescale is $(\rho_l c_l R_0^2)/k_l$, so when $R_0 = 10$ nm the dimensional time is obtained by dividing the non-dimensional value by $1.604 \times 10^{11} \mathrm{s}^{-1}$ and when $R_0 = 100$ nm by 1.604×10^9 s^{-1} **a** $\beta = 10, R_0 = 10$ nm, **b** $\beta = 10, R_0 = 100$ nm, **c** $\beta = 100, R_0 = 10$ nm, **d** $\beta = 100, R_0 = 100$ nm

final value $R = 0.2$, for $R_0 = 100$ nm the final value is $R = 0.02$). The perturbation solution is based on an expansion in terms of $\epsilon = 1/\beta$, and terms of order ϵ^2 have been neglected. We therefore expect the greatest accuracy for the large β solutions. This is clearly the case: the two curves with $\beta = 10$ are clearly less accurate than those with $\beta = 100$. However, all sets of curves show good agreement, the worst being that of Fig. 3 a) where at the final time calculated there is a difference of 3 % between the numerical and analytical results. For the best case, with $\beta = 100$, $R_0 = 100$ nm the final difference is around 0.1 %. The four graphs demonstrate that for a range of R_0 and β the evolution of the radius $R(t)$ is accurately predicted by the perturbation solution. The radius is calculated by integrating the Stefan condition, which shows $R_t \propto -T_r(R, t)$, so we can conclude that the perturbation solution for $T_r(R, t)$ is

also accurate (and in fact our numerical results demonstrate that $T(r, t)$ is also well approximated). Note that the dimensional times predicted by these calculations are of the order 10^{-11}s for the 10-nm particle and 10^{-8}s for the 100-nm particle. These fit well with the experimental values discussed in Font and Myers (2013), where particles between 2 and 20 nm melt in 'the picosecond range' whilst 50-nm particles melt 'faster than a hundred picoseconds'.

In Fig. 4, we show temperature profiles for different times as a function of r for $\beta = 100$ and $R_0 = 10, 100$ nm. Solid lines represent the temperature in the liquid, dashed lines that in the solid and the dotted line is the melt temperature variation. The solid–liquid interface follows the dotted line. For the 10-nm particle, shown in Fig. 4a, the initial melt temperature is close to 490 K. The boundary of the liquid layer does not exceed this temperature by a great amount, rising to

Fig. 4 Temperature profile of a tin nanoparticle. The *solid* and *dashed lines* represent the temperatures in the liquid and solid, respectively. The *dotted line* is the melting temperature given by the generalised Gibbs–Thomson Eq. (14). *Black horizontal line* denotes $T_H = 507.6$ K, $\beta = 100$, **a** $R_0 = 10$ nm, **b** $R_0 = 100$ nm
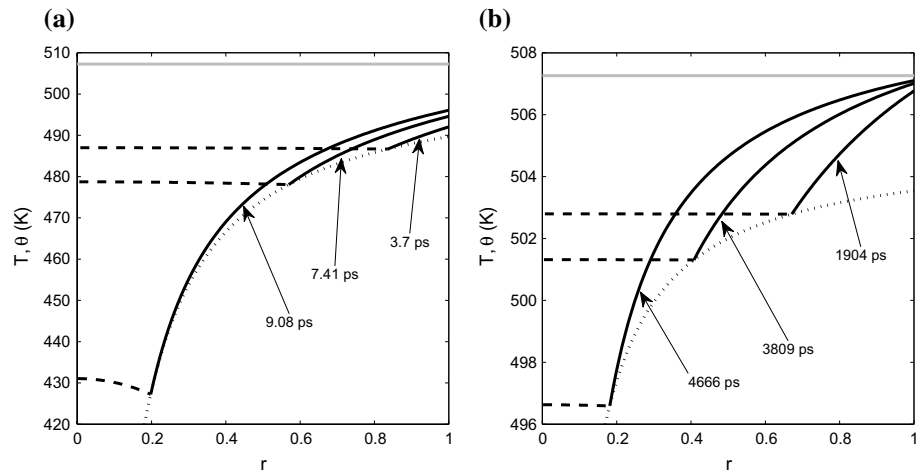
a maximum of approximately 496 K. However, by the time the boundary has reached 496 K and the melt temperature has decreased to less than 430 K. This verifies our previous statement that only a slight temperature rise above the melt temperature is required for complete melting. The curves for $t = 9.08$ ps represent the temperature profile when we expect the continuum model to break down. Here it is clear that both the solid and liquid regions are above the melt temperature. In a bulk Stefan problem, we would expect the solid to be below the melt temperature; thus, whilst the liquid temperature drives the melting, the solid acts to slow it down. In the present situation, due to the melting point depression, the solid temperature exceeds the melt temperature and so both the solid and the liquid drive the melting. This feature has been observed in previous studies of nanoparticle melting Font and Myers (2013), McCue et al. (2009). The second figure shows temperature profiles for a particle with $R_0 = 100$ nm. Now, the process takes much longer and the temperature rise at the boundary is greater.

In Fig. 5, we compare the evolution of the radius using the Stefan condition (19) [in dimensional form equation (10)] (solid line) with that of the standard Stefan condition from the literature, as described in Sect. 3, (dashed line). For an initial particle size $R_0 = 10$ nm, the current model predicts melting at almost twice the rate of the previous model. Looking at the effective latent heat definitions from the two models shows that they both have the same kinetic energy terms, so the difference must lie in the (dimensional) terms $L_m(t) + 2\sigma_{sl}^*/(\rho_s R)$ and $L_m^* + (c_l - c_s)(T_m - T_m^*)$. From Table 1, we obtain $2\sigma_{sl}^*/(\rho_s R) \approx 1.8 \times 10^{-5}/R$. This is equal to the bulk latent heat only when $R \approx 0.3$ nm, so for most of the melt process we can assume the current model predicts a melt rate of the order $R_t \propto 1/L_m(t)$. The previous model has $(c_l - c_s)(T_m - T_m^*) \approx 2000$ (if we assume a maximum temperature change of order 50 K, as shown in Fig. 4a. This is always significantly smaller than L_m^* and so the previous model predicts (approximately)
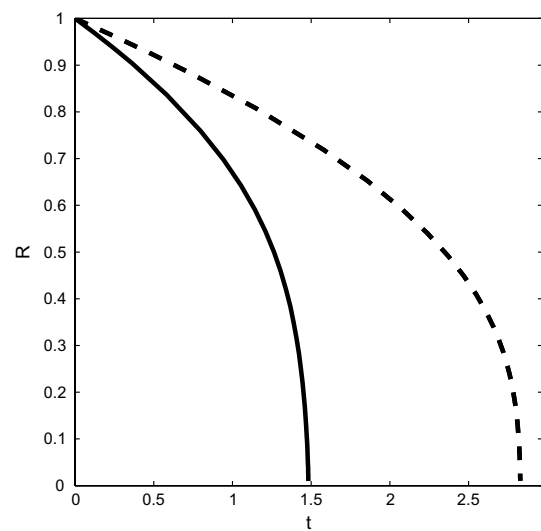

Fig. 5 Melt front position for the new (*solid line*) and old (*dashed line*) Stefan conditions, $R_0 = 10$ nm, $\beta = 100$. Dimensional times are obtained by dividing the non-dimensional value by $1.604 \times 10^{11} \mathrm{s}^{-1}$

$R_t \propto 1/L_m^*$. Given that the value of latent heat decreases by a large amount during melting, so making it easier for molecules to leave the surface, it is clear that the true melting rate must be much faster than predicted by any previous model where $R_t \propto 1/L_m^*$. Note that since $L_m(t) \to L_m^*$ as the radius increases, the difference in results will decrease with an increase in initial particle size. For example, if we carry out the same calculation as shown in Fig. 5 but set $R_0 = 100$ nm, then the difference in final melt times reduces to around 2 %. So perhaps the key point to take from this figure is that for small nanoparticles (below the size where the actual latent heat differs significantly from the bulk value) latent heat variation must be accounted for in theoretical modelling of nanoparticle melting.

In previous mathematical models, the boundary condition imposed was $T(R_b, t) = T_H$ instead of the Newton

Fig. 6 Melt front position with a Newton cooling boundary condition (*solid line*) and fixed temperature boundary condition (*dashed line*), $\beta = 100$. Dimensional times are obtained by dividing the non-dimensional value by $1.604 \times 10^{11} \text{s}^{-1}$ when $R_0 = 10$ nm and by 1.604×10^9 s^{-1} when $R_0 = 100$ nm, **a** $R_0 = 10$ nm, **b** $R_0 = 100$ nm
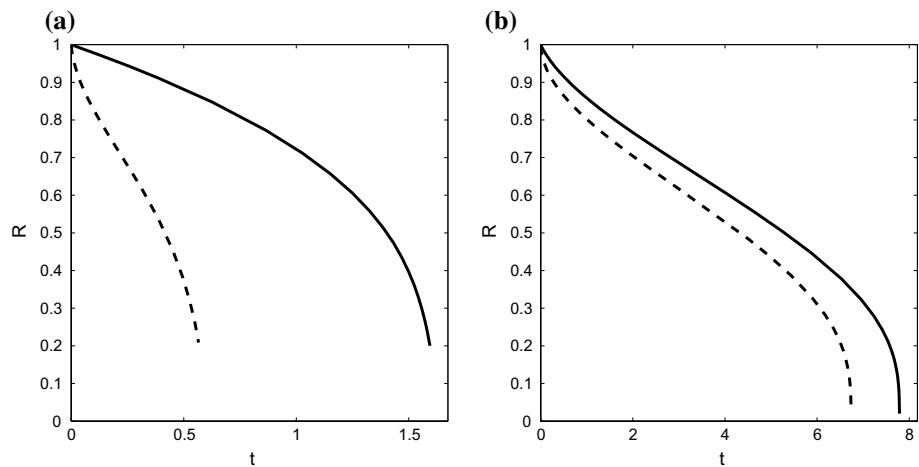
cooling condition employed in this paper. In Fig. 6, we show the difference in melting for the perturbation solution subject to the Newton cooling condition (11) (solid line) and a fixed temperature boundary condition (dashed line), both with $T_H = 507.6$ K. For the 10-nm particle, the change in boundary condition results in melting almost three times slower than with a fixed temperature. When $R_0 = 100$ nm, the melting time increases by only 13.5 %. The discrepancies may be attributed to the energy transfer to the particle. The fixed temperature boundary condition is equivalent to specifying perfectly efficient heat transfer from the surrounding material; that is, the heat transfer coefficient is infinite. Initially the particle is at some temperature below the melt temperature. At $t = 0$, the infinite heat transfer instantaneously raises the boundary temperature to T_H, and this results in an infinite temperature gradient and so, according to the Stefan condition, an infinite boundary velocity. In the figure, we see that the curve at $t = 0$ is vertical. Consequently the fixed boundary temperature model must predict faster melting than in reality. The cooling condition, even with the maximum allowable heat flux, exhibits a finite melt rate and overall slower melting.

There are further consequences of the previously employed infinite heat transfer. The liquid velocity $v(R, t) = (1 - \rho)R_t$, if $R_t(0)$ is infinite then so is $v(R, 0)$ and hence the initial kinetic energy. Let us consider the effect of the kinetic energy term on the Stefan condition (20). It is represented by $\gamma \epsilon^3 R_\tau^3$, where $\gamma \propto (1 - \rho_s/\rho_l)$ (time has been rescaled with the Stefan number). In a standard perturbation, we would neglect this term due to the small factor ϵ^3. It was retained in the current model since at least for part of the process we anticipated large R_τ. In places where the velocity is small, its contribution will be negligible and so its retention does not affect the results. If the velocity is large, then the kinetic energy term represents a considerable energy sink, resulting in slower melting. This was observed in the solutions presented in Font
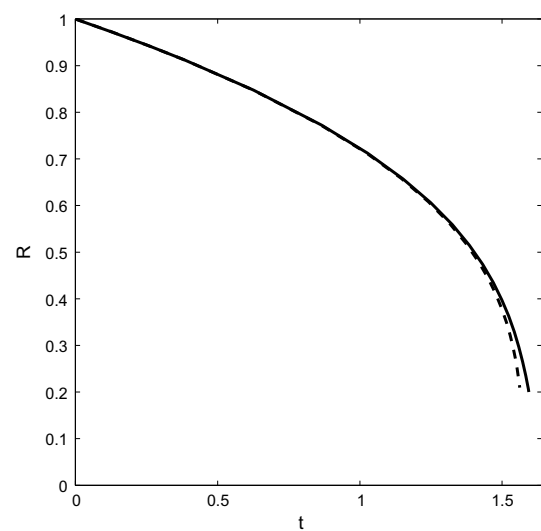

Fig. 7 Comparison of $R(t)$ for $R_0 = 10$ nm, $\beta = 100$, with and without the kinetic energy terms in the Stefan condition. Dimensional times are obtained by dividing the non-dimensional value by $1.604 \times 10^{11} \text{s}^{-1}$

et al. (2014) with a fixed temperature boundary condition and gold nanoparticles. In the present study, we have shown that the initial infinite velocity does not occur and so the initial kinetic energy is negligible. The question is then, does the high melting rate in the final stages lead to a non-negligible kinetic energy contribution? In Fig. 7, we compare results with and without the kinetic energy term for a 10-nm particle and $\beta = 100$. Clearly the difference is very small, resulting in only a 2 % change in the final melting time. We do not show the corresponding result for $R_0 = 100$ nm since the two curves are indistinguishable. This seems to indicate that the contribution of kinetic energy to the Stefan condition is negligible, which would then result in a simpler mathematical model, given that the cubic term in R_t could be removed. However, we note that

for tin $\rho = \rho_s/\rho_l = 1.028$, whereas for gold $\rho = 1.116$. In Font et al. (2014), it was stated that the inclusion of kinetic energy and density change had a significant impact on the melting process and this was so strong that it carried through to macroscale melting. From the present study, it seems their conclusion should be toned down since

1. the effect of kinetic energy is magnified by the use of a fixed temperature boundary condition;
2. the effect also depends on the solid to liquid density ratio; the higher the ratio, the greater the effect.

7 Conclusions

The work in this paper describes a model for the melting of a spherically symmetric nanoparticle. It has various novel features which appear to have important consequences for modelling at the nanoscale. Specifically it is the first mathematical model of nanoparticle melting

1. to include latent heat depression;
2. to employ the new Stefan condition developed in Myers (2016);
3. to use a Newton cooling condition.

Experimental observation and MD simulations on nanoparticle melting have made it clear that latent heat depression is significant, even more so than the well-documented melting point depression. To date, mathematical models of nanoparticle melting have accounted for the latter effect, but not the latent heat variation. In §2, we proposed an exponential model to describe published data on the latent heat variation of tin. This contained a single fitting parameter and provided much better agreement with the data than previous models in the literature, particularly when the nanoparticle size was greater than 20 nm.

Previous mathematical analyses of nanoparticle melting have imposed a fixed boundary temperature. This condition is equivalent to specifying an infinite heat transfer coefficient, which then leads to melt rates greater than occurs in practice. The present study uses a cooling condition at the boundary, and this is more physically realistic and leads to slower, finite melt rates. The decreased melt rates impact on the kinetic energy contribution. The only previous mathematical analyses of nanoparticle melting with density change employed the fixed temperature condition and concluded that the density change was very important, since the resultant kinetic energy provides an energy sink which then reduces the energy available to drive the phase change. This effect was so strong that it carried through even to the macroscale. Their study used data for gold, which has a large difference between liquid and solid density. Our work, which uses data for tin (with a density ratio close to unity) and a heat flux of the order of the maximum possible value for thermodynamic stability indicated a much smaller influence of kinetic energy. This is attributed primarily to the new boundary condition, which removes the initial infinite melt rate (and corresponding infinite kinetic energy). The choice of maximum possible heat flux was to permit comparison with results from the literature; in practice, one would use a smaller value and so, in general, kinetic energy would be even lower than in our calculations. Consequently, our results indicate that provided the density difference is not large and the boundary condition is physically realistic then the contribution of kinetic energy to the Stefan condition may be neglected. This will then considerably simplify the formulation, allowing the removal of the cubic velocity term.

The mathematical model contained two other novel features, namely the latent heat variation and the new Stefan condition. Both of these play a role in the melting behaviour, although since latent heat is the dominant term for most of the process it is the latent heat variation that appears to be the most important.

One final point to note is that in previous studies of nanoparticle melting, the speed of melting of small particles was close to the relaxation time for the material. When we include latent heat variation, this melting time decreases even further (the cooling condition has some effect in slowing down melting, but is not as strong as the latent heat effect). This indicates that in future models it would be sensible to investigate non-classical heat equations which hold over very short timescales.

References

Ahmad F, Pandey AK, Herzog AB, Rose JB, Gerba CP, Hashsham SA (2012) Environmental applications and potential health implications of quantum dots. J Nanoparticle Res 14:1038

Alexiades V, Solomon AD (1992) Mathematical modeling of melting and freezing processes. Hemisphere, Washington DC

Bachels T, Güntherodt H-J, Schäfer R (2000) Melting of isolated tin nanoparticles. Phys Rev Lett 85:1250–1253

Back JM (2014) Stefan Problems for Melting Nanoscaled Particles, PhD thesis, U. Queensland. http://eprints.qut.edu.au/79905/1/Julian_Back_Thesis. Accessed 12 Aug 2016

Back JM, McCue SW, Hsieh MH-N, Moroney TJ (2014) The effect of surface tension and kinetic undercooling on a radially-symmetric melting problem. Appl Math Comput 229:41–52

Back JM, McCue SW, Moroney TJ (2014) Including nonequilibrium interface kinetics in a continuum model for melting nanoscaled particles. Sci Rep 4:7066

Buffat P, Borel J-P (1976) Size effect on the melting temperature of gold particles. Phys Rev A 13:2287–2298

David TB, Lereah Y, Deutscher G, Kofman R, Cheyssac P (1995) Solid–liquid transition in ultra-fine lead particles. Philos Mag A 71:1135–1143

Delogu F (2005) Structural and energetic properties of unsupported Cu nanoparticles from room temperature to the melting point: molecular dynamics simulations. Phys Rev B 72:205418

Dieringer JA, McFarland AD, Shah NC, Stuart DA, Whitney AV, Yonzon CR, Young MA, Zhang X, Van Duyne RP (2006) Introductory lecture: surface enhanced Raman spectroscopy: new materials, concepts, characterization tools, and applications. Faraday Discuss 132:9–26

Dragomirescu FD, Eisenschmidt K, Rohde C, Weigand B (2016) Perturbation solutions for the finite radially symmetric Stefan problem. Int J Therm Sci 104:386–395

Ercolessi F, Andreoni W, Tosatti E (1991) Melting of small gold particles: mechanism and size effects. Phys Rev Lett 66:911–914

Fedorov AV, Shulgin AV (2011) Mathematical modeling of melting of nano-sized metal particles. Combust Explos Shock Waves 47(2):147–152

Florio BJ, Myers TG (2016) The melting and solidification of nanowires. J Nanoparticle Res 18(6):1–12

Font F, Myers TG (2013) Spherically symmetric nanoparticle melting with a variable phase change temperature. J Nanoparticle Res 15:2086

Font F, Myers TG, Mitchell SL (2014) A mathematical model for nanoparticle melting with density change. Microfluid Nanofluidics 18:233–243

Garg S, Bansal R, Ghosh C (1993) Thermal physics. Tata McGraw-Hill Education, New Delhi

Gröhn F, Kim G, Bauer BJ, Amis EJ (2001) Nanoparticle formation within dendrimer-containing polymer networks: route to new organic-inorganic hybrid materials. Macromolecules 34:2179–2185

Jiang H, Moon K-S, Dong H, Hua F, Wong C (2006) Size-dependent melting properties of tin nanoparticles. Chem Phys Lett 429:492–496

Jou D, Casas-Vázquez J, Lebon G (1996) Extended irreversible thermodynamics. Springer, Berlin

Lai S, Guo J, Petrova V, Ramanath G, Allen L (1996) Size-dependent melting properties of small tin particles: nanocalorimetric measurements. Phys Rev Lett 77:99–102

Latent Heat of Melting of some common Materials. http://www.engineeringtoolbox.com/latent-heat-melting-solids-d_96.html. Accessed 19 Nov 2015

Lim HS, Ong CK, Ercolessi F (1993) Surface effects in vibrational and melting properties of Pb clusters. Zeitschrift für Phys D Atoms Mol Clust 26:45–47

McCue SW, Wu B, Hill JM (2009) Micro/nanoparticle melting with spherical symmetry and surface tension. IMA J Appl Math 74:439–457

Mornet S, Vasseur S, Grasset F, Duguet E (2004) Magnetic nanoparticle design for medical diagnosis and therapy. J Mater Chem 14:2161

Myers TG, Mitchell SL, Font F (2012) Energy conservation in the one-phase supercooled Stefan problem. Int Commun Heat Mass Transf 39(10):1522–1525

Myers TG, MacDevette MM, Font F, Cregan V (2014) Continuum mathematics at the nanoscale. J Math Ind 4(1):1–13

Myers TG (2016) Mathematical modelling of phase change at the nanoscale. Int Commun Heat Mass Transf 76:59–62

Salata O (2004) Applications of nanoparticles in biology and medicine. J Nanobiotechnol 2:3

Sharafat S, Ghoniem N (2000) Summary of thermo-physical properties of Sn, and compounds of Sn-H Sn-O, Sn-C, Sn-Li, Sn-Si Comp. Prop. Sn, Sn-Li, Pb-Li, Rep. UCLA-UCMEP-00-31, University of California, Los Angeles

Shin J-H, Deinert MR (2014) A model for the latent heat of melting in free standing metal nanoparticles. J Chem Phys 140:164707

Sun J, Simon S (2007) The melting behavior of aluminum nanoparticles. Thermochim Acta 463:32–40

Tanabe K (2007) Optical radiation efficiencies of metal nanoparticles for optoelectronic applications. Mater Lett 61:4573–4575

Thermal Conductivity of Materials and Gases. http://www.engineeringtoolbox.com/thermal-conductivity-d_429.html. Accessed 19 Nov 2015

Tolman RC (1949) The effect of droplet size on surface tension. J Chem Phys 17:333

Wu B, Tillman P, McCue SW, Hill JM (2009) Nanoparticle melting as a Stefan moving boundary problem. J Nanosci Nanotechnol 9(2):885–888

Wu B, McCue SW, Tillman P, Hill JM (2009) Single phase limit for melting nanoparticles. Appl Math Model 33(5):2349–2367

Xiong S, Qi W, Cheng Y, Huang B, Wang M, Li Y (2011) Universal relation for size dependent thermodynamic properties of metallic nanoparticles. Phys Chem Chem Phys 13:10652–10660

Yih TC, Al-Fandi M (2006) Engineered nanoparticles as precise drug delivery systems. J Cell Biochem 97:1184–1190

Zhang M, Efremov M, Schiettekatte F, Olson E, Kwan A, Lai S, Wisleder T, Greene J, Allen L (2000) Size-dependent melting point depression of nanostructures: nanocalorimetric measurements. Phys Rev B 62:10548–10557

Zhang Y, Zhang HL, Wu JH, Wang XT (2011) Enhanced thermal conductivity in copper matrix composites reinforced with titanium-coated diamond particles. Scr Mater 65(12):1097–1100